

# Properties of Additively Manufactured Deposits of Alloy 718 Using CMT Process Depending on Wire Batch and Shielding Gas

*Manuela Zinke, Stefan Burger and Sven Juettner*

## Abstract

Wire + arc additive manufacturing (WAAM®) is a versatile, low-cost, energy-efficient technology used in metal additive manufacturing (AM). This process uses arc welding to melt a wire and form a three-dimensional (3D) object using a layer-by-layer deposit. In the present study, the effect of heat input and shielding gas during CMT-WAAM welding on cooling time, mechanical properties at room temperature, and macro- and microstructure was investigated based on different part geometries (wall, block) using two S Ni 718 wire batches. The heat input and consequently the cooling rate were varied by changing the wire feed and the travel speed. As expected, increasing the heat input leads to higher cooling times. Due to the 2D-heat conduction, the thin walls cool significantly slower than the multi-pass block welds. Nevertheless, the influence on mechanical properties is only marginal. Both the AM batch of S Ni 718 with the lower Nb/C and the multi-pass block welds with the higher thermomechanical reactions exhibit a high susceptibility to unacceptable seam defects, such as hot cracks or lacks of fusion. But even the standard batch causes hot cracks. An influence of the shielding gas on microstructure, mechanical properties, and occurrence of the seam defects cannot be detected.

**Keywords:** additive manufacturing, alloy 718, wire batch, shielding gas, cooling time, seam defects, mechanical properties, hardness, microstructure

## 1. Introduction

Superalloy Alloy 718 (NiCr19NbMo, EN 2.4668) is a Ni-Cr-Fe-Mo alloy for service conditions up to 650°C, where hardening is achieved by additions of Nb, Ti, and Al resulting in controlled precipitation of mainly  $\gamma''$  (Ni<sub>3</sub>Nb) and to a small extent  $\gamma'$  (Ni<sub>3</sub>(Al, Ti) [1]. Due to this, this alloy is widely used for static and rotating components in stationary gas turbines, rocket drives and spacecraft, motor vehicle

turbo chargers, high-strength screws, springs and mounting elements, and for heat-resistant tools in forgeries, extruders, and separating shearers [2].

Ni-alloys have a high cost and are difficult to machine, with main reasons being their high temperature resistance, high initial work hardening rate, and presence of carbides in the microstructure [3]. Therefore, additive manufacturing (AM) techniques could result in cost, weight, and machining savings for a wide range of applications using Alloy 718 [4]. The AM with wire-based arc processes (WAAM®) offers the possibility of producing small and large-volume components of low and medium complexity at high deposition rates. A disadvantage is the poorer surface quality and accuracy and thus the need for mechanical finishing of functional surfaces [5–7]. A typical process for WAAM® is the energy-reduced Cold Metal Transfer (CMT) process, a variant of GMAW, which is widely used industrially for cladding with Ni-base solid wires [8–11]. This is due to the very low dilution with substrate, high deposition rate, very low heat input, less spatter, and low susceptibility to hot cracking [12], factors that are also advantageous for AM.

Recently, the number of publications on AM of Alloy 718 with the GMAW is increasing [13] published a study as early as 2007 on the use of the MIG process for AM of an internal flange of combustor outer casing of Alloy 718. The present study has highlighted the presence of deleterious Laves- and  $\delta$  phases in the weld deposition structures encouraged by extended time at high temperature during either deposition or subsequent post-deposition heat treatment. In addition, associated discontinuities in the form of hot cracks and shrinkage porosity have been identified [14, 15] evaluated the effect of oxide, wire source, and heat treatment on the mechanical properties of additive plasma arc welding with cold wire feed of Alloy 718 with oscillating torch in inert shielding gas atmosphere. Results showed that oxides formed during deposition had no effect on the mechanical properties. Wires from different suppliers resulted in around 50 MPa difference in UTS. Standard heat treatment improved the strength from 824 MPa to 1110 MPa, but the average strength was lower than the wrought alloy and laser powder-based AM IN718. The microstructure of the WAAM material showed large columnar grains and numerous Laves phase [16] identified an aging effect in deposits of Alloy 718, which produced with CMT-WAAM® process. Deposits consisting of 10 layers were manufactured, where interpass time (0, 30 s, and 60 s) was the only process parameter varied. An aging effect was observed, which caused precipitation of the  $\gamma''$  and  $\gamma'$  strengthening phases and the  $\delta$  phase. The highest hardness value was measured in the middle section of each deposit due to precipitation of the strengthening phases [4] investigates the effects of processing parameters and heat treatments employed on CMT-WAAM® of Alloy 718. The process stability was analyzed by electrical transients and melt pool imaging, showing an opposite trend to the measured heat inputs. Laves length and carbide diameter decreased with travel speed, while the as-deposited hardness increased. These observations permitted a linear wall to be fabricated with a minimal heat input per layer of 181 J–185 J/mm. Compared with powder-based AM, the CMT welds exhibit a larger melt pool size and lower as-deposited hardness, but has been found to show satisfactory aging response and similar Laves phase area fraction.

In the present work, the influence of different heat inputs and shielding gases in CMT-WAAM with S Ni 7718 on the macrostructure, seam defects, chemical composition, mechanical properties, and hardness was investigated. The investigations were carried out with two different wire batches on two component geometries (wall and block). These different geometries generate different welding situations (single- or multi-bead welding) and stress conditions.

## 2. Experimental setup

For WAAM®, two welding equipment were used: a three-axis gantry machine with programmable logic controller (PLC) and a two-axis welding portal FCB 900–500/ML100 (**Figure 1**). To achieve a low heat input (E), the welds were made using the Cold Metal Transfer (CMT) process of the company Fronius. For logistical reasons, two power sources (PS) were used with the RCU 5000 control unit: CMT TPS 4000, first generation (PS 1) and CMT Advanced 4000, second generation (PS 2). However, the welds were made with the same synergy line (NIBAS 625/1.2mmM12 Ar + 2,5% CO<sub>2</sub>). Accompanying the welds, the electrical welding parameters, the shielding gas flow, and the wire feed speed were recorded and monitored with external measuring system WeldAnalyst-S2 (HKS Prozesstechnik GmbH). During the welding process, infrared pyrometers were used to measure the temperature of the welded parts. Two batches of solid wire S Ni 7718 from different manufacturers with diameter 1.2 mm were used. One of them is a standard batch, while the other is made specifically for AM.

## 3. Deposition strategy

Since in additive welding, the parts geometry influences the cooling rate and thus the microstructure and mechanical properties, in a first step, two different part geometries (thin wall and multi-pass block) were initially investigated (**Figure 2**).

Depending on the geometry, different substrate sheets were used. These sheets were welded to a 40 mm thick carbon steel plate to counteract distortion and produce high thermomechanical reactions. For welding of both geometries, a stick-out of 15 mm and 30% He, 2% H<sub>2</sub>, 0.05% CO<sub>2</sub>, bal. Ar as shielding gas with a flow rate of 18 l/min were used. This gas is recommended for welding Ni alloys, as it ensures good flow and wetting behavior of the highly viscous melt. During the welding, the direction was changed after each layer. Between the beads or layers, there was no brushing. For all welds, the maximum interpass temperature (IT) was 150°C. To influence the deposition rate and heat input at welding the walls, the wire feed speed (WFS) was varied between 6.0 and 9.0 m/min and the travel speed (TS) between 0.6 and 1.0 m/min. To achieve a high deposition rate when manufacturing multi-pass block with stringer bead technique, a high wire feed speed (WFS: 9.0 resp. 9.5 m/min) and a low welding speed (TS: 0.6 m/min) were selected.

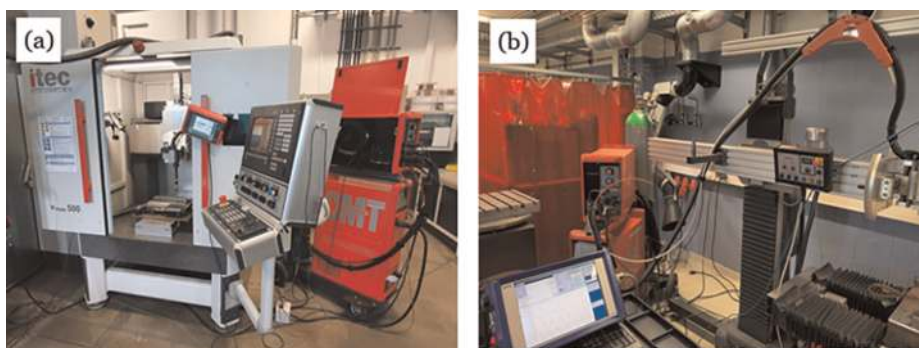


**Figure 1.** Experimental setup for additively GMAW (a) three-axis gantry machine with CMT advanced 4000 and (b) two-axis welding portal with CMT TPS 4000.

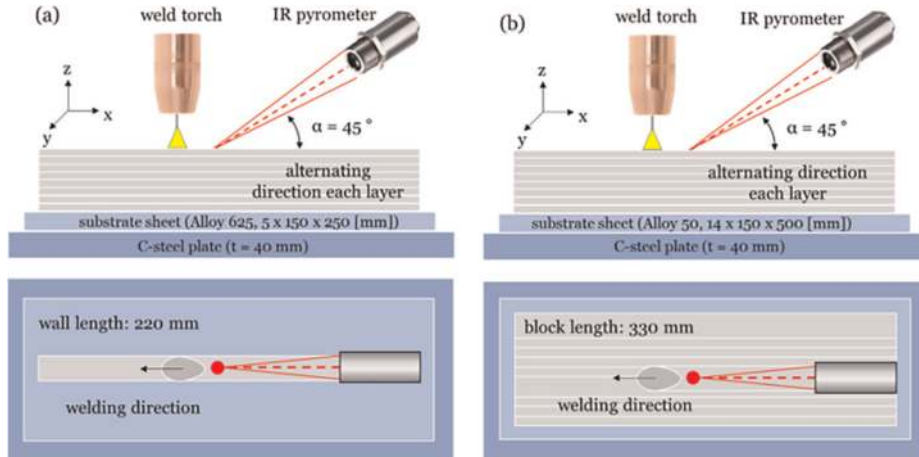


**Figure 2.** Deposition strategy of (a) wall (b) block (above: side view, below: top view).

In second step, the influence of different shielding gases on the seam quality was investigated. Ni-alloys are normally welded with inert shielding gas. Additions of active gases ( $\text{CO}_2$ ,  $\text{O}_2$ ) in the ppm range and of He or  $\text{H}_2$  improve the flow and wetting behavior of the melt. However, the presence of  $\text{CO}_2$  or  $\text{O}_2$  can also lead to a slight seam oxidation. This effect can increase the possibility of lack of fusion on multi-pass deposition. On the other hand, hydrogen has a reducing effect and can ensure an oxide-free seam appearance. The following shielding gases were used:

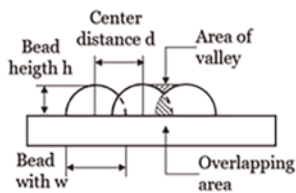
- bal. Ar/30% He/2%  $\text{H}_2$ /0,055% $\text{CO}_2$  (ArHeHC)
- bal. Ar/30% He/1%  $\text{H}_2$  (ArHeH)
- bal. Ar/2%  $\text{H}_2$  (ArH)
- bal. Ar/30% He/0,03%  $\text{O}_2$  (ArHeO)

These investigations were also performed on walls and blocks with constant setting values (WFS: 9.0 resp. 9.5 m/min and TS: 0.6 m/min). The nominal dimensions were for walls 200 mm long and 60 mm high and for blocks 200 mm long and circa 25 mm–30 mm high and 30 mm–35 mm wide. In contrast to the previous blocks, the welding direction was changed after each stringer bead. The remaining welding conditions (stick-out, IT, etc.) corresponded to the previously tests.

In multi-pass deposition, maintaining the correct center distance  $d$  between stringer beads is of elementary importance. If this distance is too big, there is no connection to the neighboring bead and lack of fusion can occur. If it is too small, the beads overlap too much and no even seam surface is created. Therefore, it is important to ensure that the overlap areas and valleys are of equal size. In [17] it is proposed to calculate the ideal center distance depending on the ratio of WFS/TS. If WFS/TS > 12.5, the equations shown in **Figure 3** should be used.

#### 4. Test methods

First the exact characterization of the wire electrodes took place. To determine the chemical composition, the wires were melted into buttons with the Arc Melter



$$d = \frac{1}{2h} (2R^2 \arcsin\left(\frac{w}{2R}\right) + wh - wR) \quad \text{Eq. 1}$$

$$\text{with } R = \frac{(h^2 + \frac{w^2}{4})}{2h} \quad \text{Eq. 2}$$

**Figure 3.** Illustration of overlapping beads and equations for calculating the ideal center distance [16].

MAM-1 (Edmund Bühler GmbH) in pure argon atmosphere (99.996%) using a TIG arc. The methodology is described in [18]. The chemical composition of buttons was analyzed with the atom emission spectrometry (AES). In addition, the contents of oxygen, nitrogen, carbon, and sulfur were measured by means of carrier gas melt extraction (CGME) with combustion analysis (CA) directly on the solid wire in the delivery condition. Afterward, measurements of the wire diameter, the surface roughness (axial) with the tactile cut method [19], and tensile tests were carried out.

The welded components have been subjected to a visual and dye penetration test. In the first step, the metallographic cross sections (Y-Z plane) are taken. For the automatic preparation, it was necessary to cut the cross sections in the middle. All samples were processed with standard metallographic techniques with a final polish of 0.5 μm O.P.S (SiO<sub>2</sub>). Subsequently, the central part of the walls and blocks were mechanically machined to allow high-quality X-ray inspection. While the image quality indicator according to [20] on the walls was 16 or 17, only an indicator of 10 was achieved on the blocks due to their higher thickness. For this reason, no radiographic testing was performed on the blocks. On walls and blocks, chemical analyses, tensile tests, and hardness measurements were performed. Standard tensile tests were performed to BS EN ISO 6892-1 [21] at room temperature. The tensile specimens with form E 5 x10 × 40 [22] were taken in welding direction. Vickers hardness testing was performed in compliance with BSEN ISO 6507-1 [23], using a load of 0.2 or 10 kg. Measurements were made at varying distances from the substrate. Only on the blocks the determination of the impact energy on Charpy V samples at room and low temperatures (−196°C) was carried out. The microstructure was investigated by light optical microscope (inverse incident light microscope Leica MeF4A, Leica), scanning electron microscope (XL30 FEG/ESEM, company FEI/Philips), and energy-dispersive spectrometer (EDAX Si (Li) detector).

## 5. Results and discussion

### 5.1 Characterization of wire batches

The chemical compositions of S Ni 7718 wire batched are listed in **Table 1**. The AM batch has lower contents of Cu and Co. Furthermore, it has slightly higher contents of C, Nb, and Fe than the standard variant. These elements influence the precipitation of the Laves phase, MC-type carbides, and TN in the weld metal [24–26]. Furthermore, the solidification cracking of austenitic materials is strongly dependent on the solidification temperature range (STR) and especially the solidification at the grain boundaries and interdendritic regions. The Nb/C ratio affects the amount and distribution of the γ + NbC eutectic and γ + Laves eutectic, which influence the STR. Addition of Nb at higher C levels promoted γ/NbC eutectic type constituent and at higher Si and Fe

Element	C	Si	S	Cr	Mo	Fe	Nb	Al	Ti	Cu	Co	Ni	Nb/C
Standard	0.04	0.06	0.001	19.1	2.6	17.9	5.67	0.53	1.12	0.05	0.07	52.6	149
AM	0.07	0.04	0.001	18.0	2.7	20.2	5.99	0.52	1.16	<0.01	<0.01	5.12	89

**Table 1.**  
Chemical composition of different wire batches of S Ni 7718 (wt%).

Parameter	Ø [mm]	Surface	Rz [µm]	UTS [MPa]	A <sub>50mm</sub> [%]
Standard	1.19	matt	1.38 ± 0.05	1407 ± 22	4.6 ± 0.4
AM	1.18	glossy	0.47 ± 0.04	1326 ± 30	9.8 ± 0.3

**Table 2.**  
Mechanical properties at RT and roughness of solid wire electrodes.

levels promoted  $\gamma$ /laves [27]. When Nb/C ratio was increasing, the solidification temperature range (STR) was reduced [28].

A basic requirement of a stable gas-metal arc welding process is a permanently constant feed of the wire electrode, even with cable assembly of different lengths. The main factors influencing this are the surface condition of the wire electrode, mechanical properties, and also technological characteristics. Basically, the wire electrode for GMAW should have a high tensile strength (UTS) with sufficient elongation at rupture (A) to ensure high stiffness even in long cable assemblies [29]. Both wire variants guarantee these requirements (**Table 2**). For the sliding behavior in long hose assemblies, the basic rule is that with lower roughness (Rz) and greater pre-bending, the sliding ability of wire electrodes in the hose assembly increases [30]. The AM variant has a lower average roughness values, which also correlate with the appearance of the wire surface. Despite the different properties and characteristics, no significant influence on the wire feeding and thus on the process behavior was found under the selected test conditions.

## 5.2 Heat input and deposition rate

An arithmetic mean value for all weld beads of the wall or block was formed from the mean value of the respective stringer bead read off the power sources. The tolerance given is the average of the positive and negative error indicators. The heat input (E) is the quotient of arc power ( $P_{arc} = I \times U$ ) and travel speed (TS). The deposition rate (DR) is the amount of wire melted per unit time. Despite the same synergic line and setting parameters, differences in the measured values for current (I) and voltage (U) occurred for both current sources and consequently in the heat input (E) and deposition rate (DR) when producing the walls (**Table 3**). The large blocks were welded only with a high wire feed speed and a low welding speed to generate a high deposition rate (**Table 4**).

Moreover, this combination represents the critical case, since the heat input is comparatively high. Fourteen layers of nine stringer beads per layer each were made. Due to the long production time of 10.5 hours resulting from the interpass temperature, only one block was welded at a time. The welding time was only 70 minutes.

**Tables 5 and 6** show the weld parameters of walls and blocks welds with the varied shielding gases. It can be seen that the shielding gas has a slight influence on these

Wire batch	Setting values				Mean values		
	WFS [m/min]	TS [m/min]	I [A]	U [V]	WFS [m/min]	E [J/mm]	DR [kg/h]
Standard/PS1	6.0	0.6	133 ± 2.0	15.3 ± 0.2	6.3 ± 1.2	203 ± 5.7	3.53
		1.0	144 ± 3.0	17.0 ± 1.4	6.8 ± 0.8	147 ± 9.1	3.83
	9.0	0.6	208 ± 3.0	19.9 ± 0.6	9.7 ± 1.2	414 ± 9.4	5.44
		1.0	204 ± 3.0	19.7 ± 1.0	9.8 ± 1.0	241 ± 11.1	5.50
AM/PS2	6.0	0.6	123 ± 2.3	15.6 ± 1.1	4.9 ± 0.8	192 ± 13.7	2.74
		1.0	120 ± 4.5	16.1 ± 0.6	5.0 ± 1.0	115 ± 6.1	2.78
	9.0	0.6	178 ± 2.5	21.8 ± 0.6	7.4 ± 1.2	388 ± 8.9	4.16
		1.0	167 ± 3.5	19.9 ± 0.5	8.2 ± 1.6	200 ± 6.0	4.58

**Table 3.**  
 Welding parameters for CMT-WAAM® of walls, welded with ArHeHC.

Wire batch	Setting values				Mean values		
	WFS [m/min]	TS [m/min]	I [A]	U [V]	WFS [m/min]	E [J/mm]	DR [kg/h]
Standard/PS2	9.0	0.6	159 ± 18.5	22.2 ± 7.6	8.6 ± 2.0	352 ± 49	4.82
Am/PS2	9.5	0.6	174 ± 22.0	22.0 ± 7.5	8.7 ± 1.1	382 ± 56	4.88

**Table 4.**  
 Welding parameters for CMT-WAAM® of blocks, welded with ArHeHC.

Shielding gas	Wall				Block			
	I [A]	U [V]	WFS [m/min]	E [J/mm]	I [A]	U [V]	WFS [m/min]	E [J/mm]
ArHeHC	218 ± 4.4	21.1 ± 0.6	10.3 ± 0.4	461 ± 20	216 ± 9.7	20.9 ± 1.6	10.1 ± 0.7	451 ± 34
AeHeH	217 ± 3.6	20.5 ± 0.6	10.2 ± 0.3	445 ± 18	216 ± 5.0	19.8 ± 1.6	10.0 ± 0.5	429 ± 34
ArH	216 ± 1.7	19.6 ± 0.3	10.2 ± 0.2	423 ± 7	212 ± 6.2	19.3 ± 1.9	9.8 ± 0.8	409 ± 40
AeHeO	214 ± 3.4	19.2 ± 0.2	9.9 ± 0.2	416 ± 11	212 ± 7.2	19.2 ± 1.2	9.6 ± 0.7	407 ± 26

**Table 5.**  
 Mean values for CMT-WAAM® welds (standard batch, PS1, WFS: 9.0 m/min, TS: 0.6 m/min).

Shielding gas	wall				block			
	I [A]	U [V]	WFS [m/min]	E [J/mm]	I [A]	U [V]	WFS [m/min]	E [J/mm]
ArHeHC	217 ± 3.8	20.3 ± 0.8	1.4 ± 10.5	439 ± 15	215 ± 6.6	19.6 ± 1.7	10.1 ± 1.0	422 ± 34
AeHeH	217 ± 4.0	19.8 ± 0.5	10.5 ± 0.8	430 ± 16	214 ± 7.4	18.9 ± 1.4	9.8 ± 0.6	405 ± 35
ArH	215 ± 4.1	18.8 ± 0.9	9.8 ± 0.7	404 ± 24	209 ± 6.8	18.0 ± 1.9	9.4 ± 0.8	375 ± 48
AeHeO	214 ± 3.8	18.3 ± 1.2	9.7 ± 0.3	392 ± 29	215 ± 7.1	17.8 ± 0.8	9.6 ± 0.4	383 ± 40

**Table 6.**  
 Mean values for CMT-WAAM® welds (AM batch, PS1, WFS: 9.5 m/min, TS: 0.6 m/min).

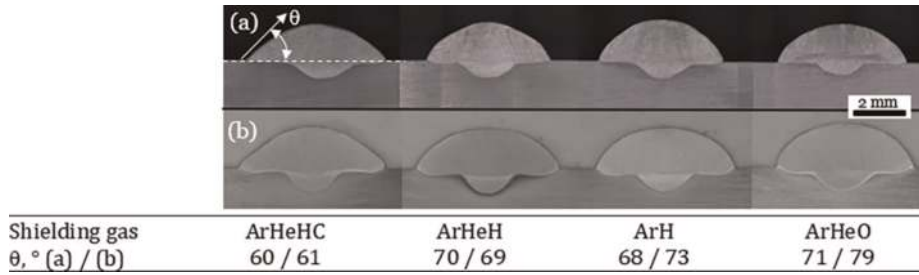


**Figure 4.** Cross sections of stringer beads depending on shielding gas: (a) standard batch (b) AM batch.

parameters. The lowest heat input is generated when ArHeO is used, while ArHeHC results in the highest values.

Cross sections of stringer beads as a function of shielding gas show the lowest wetting angles  $\theta$  when ArHeHC is used (**Figure 4**). This gas caused the highest heat input. The wetting angle increases with all other shielding gases. A low wetting angle has a positive effect on reducing lack of fusion in multi-pass welds.

### 5.3 Cooling time

Infrared (IR) pyrometers were used to measure the temperatures directly on the seam surface for every second layer at the wall structures. Since there is no specific temperature interval for the cooling time for Ni-based materials, this was calculated for cooling from 1000–600°C. **Figure 5** shows the cooling times  $t_{10/6}$  depending on heat input and layer for both batches when welding the walls. In the first layers, shorter cooling times occur due to the still possible heat conduction into the substrate. From about the 10th layer, the 3D changes to a 2D-heat conduction, which is why the cooling time remains almost constant. As expected, the cooling times increase with increasing heat input when welding the walls. At the highest heat energy of 414 J/mm, the cooling time is about 21 s. And at the lowest heat input of 105 J/mm, the cooling time is about 7 s.

The blocks cool significantly faster at comparable setting values and similar heat input due to the 2D-heat conduction. This is shown as an example in **Figure 6a** for the S Ni 7718 AM. The average  $t_{10/6}$  times are approximately between 4 s and 5 s. The further layers then cool down somewhat more slowly. In addition, it can be observed that the outer beads of each layer in the upper layers also usually cool down somewhat slower than the inner beads (**Figure 6b**).

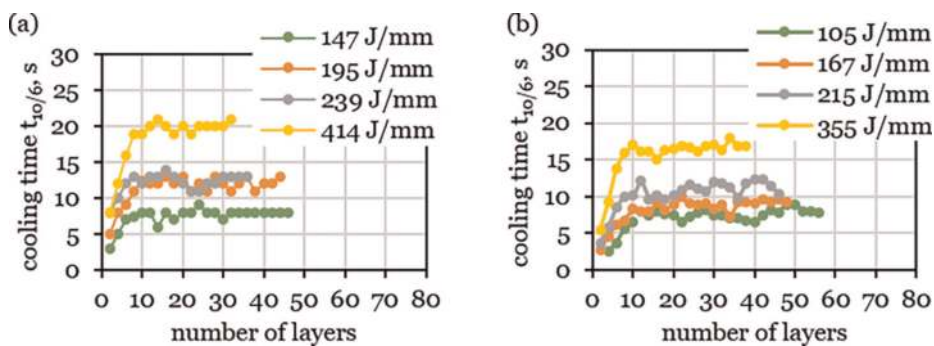


**Figure 5.**  $t_{10/6}$  cooling times of S Ni 7718 walls: (a) standard batch (b) AM batch depending on number of layers and heat input (shielding gas: ArHeHC).

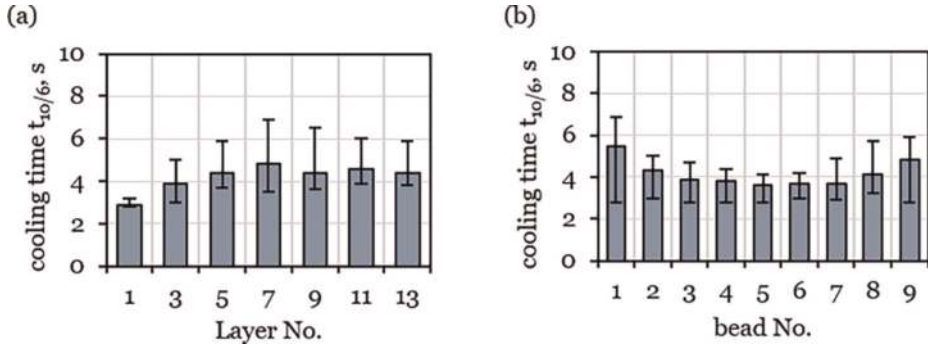


**Figure 6.** Mean  $t_{10/6}$  cooling times of S Ni 7718 AM blocks depending on (a) layer and (b) bead (shielding gas: ArHeHC).

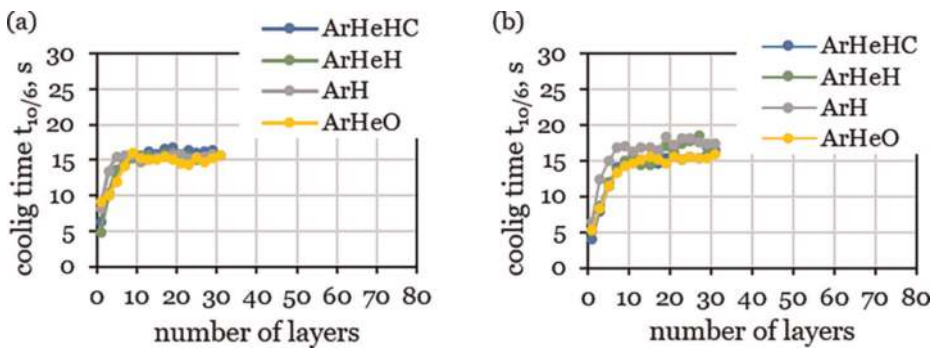


**Figure 7.**  $t_{10/6}$  cooling times in walls of S Ni 7718: (a) standard batch and (b) AM batch depending on number of layers and shielding gas.

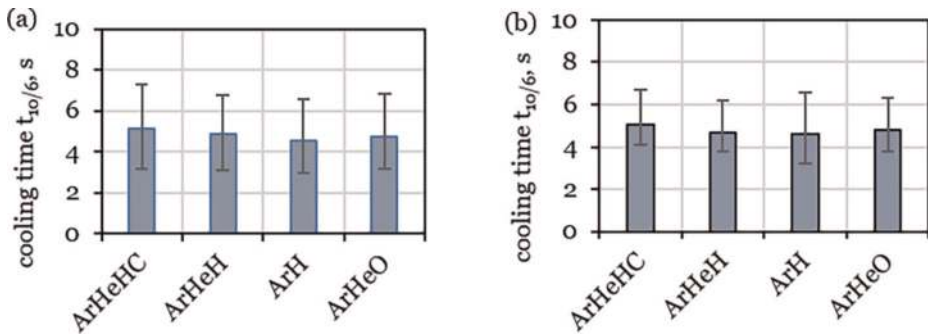


**Figure 8.** Mean  $t_{10/6}$  cooling times in blocks of S Ni 7718 depending on shielding gas: (a) standard batch (b) AM batch.

The shielding gas exerts only a minor influence on the cooling time, since the amounts for the heat input do not differ significantly (Figures 7 and 8).

#### 5.4 Nondestructive testing

As a result of the visual inspection, no external defects such as cracks, lack of fusion or pores were observed. Only some welds of the standard charge of S Ni 7718 with shielding gases containing active gas components ( $\text{CO}_2$  and  $\text{O}_2$ ) showed dark particles on the weld surfaces (Figure 9).

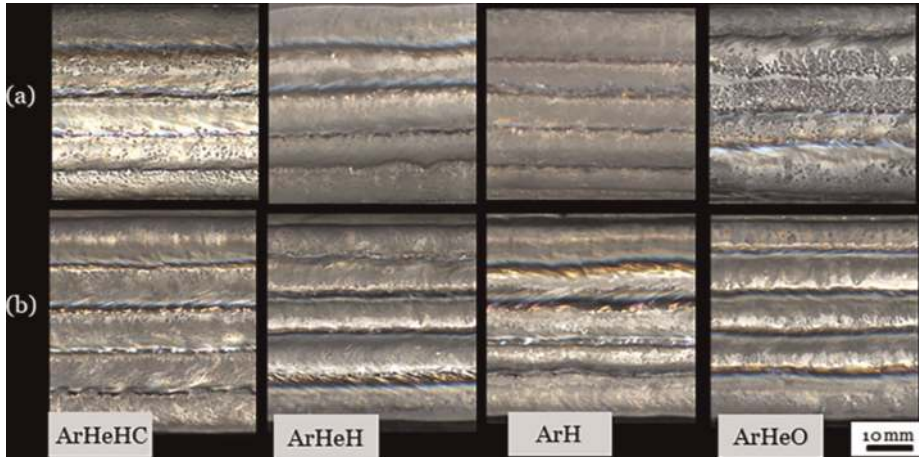


**Figure 9.** Surfaces of S Ni 7718 blocks depending on shielding gas: (a) standard batch (b) AM batch.

It is assumed that metallurgical reactions with the oxygen-affine elements Al or Cr occur due to the size of the molten pool and slow cooling. On the stringer beads' surfaces of welded walls fabricated with higher heat input, these particles also occurred, but in both wire batches. However, no deterioration of the CMT process stability was observed.

The penetration tests on walls and blocks resulted in some red indications independent of wire and welding speed (**Figure 10**).

On the cross sections of walls, it was determined that these defects always occur in the last welded layer of walls and in some cases extend to the surface (**Figure 11**). Due to their structure and dimensions, these phenomena are not classified as solidification cracks or pores but as micro blowholes. Since the components are subsequently machined, these defects are not significant.

The X-ray examinations showed no or very small porosity of less than 0.001%. The porosity is the quotient of the sum of the areas of all pores and the X-rayed weld metal area. **Figure 12** shows an X-ray image of a wall with one pore. No radiographic tests were performed on the blocks due to the low image quality number, as they did not provide sufficient information.



**Figure 10.** Example of penetration test of last layer surface with red indications.

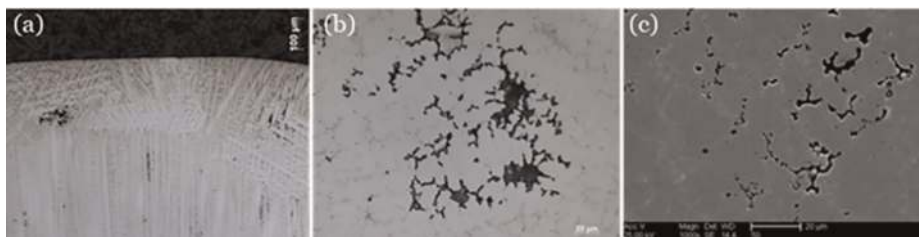


**Figure 11.** Cross sections (Y-Z plane) with examples for micro blowholes: (a) 100x magnification (b) and (c) 1000fach.

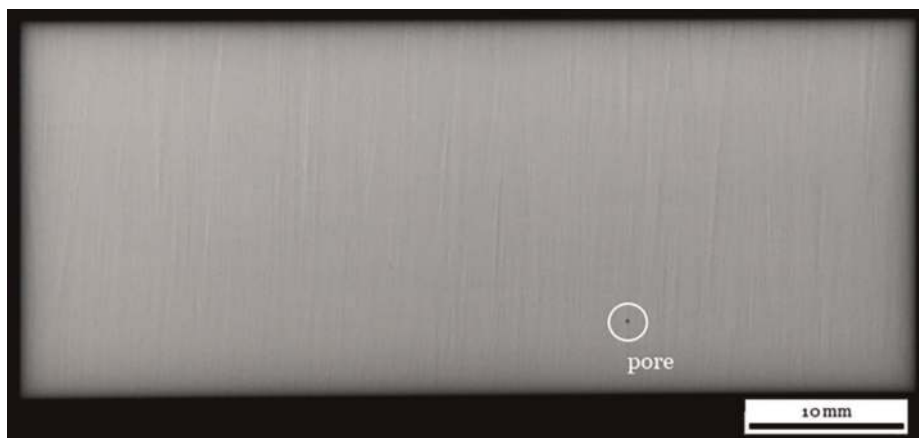


**Figure 12.**  
 X-ray test on the example of S N 7718 AM wall welded with ArH.

## 5.5 Chemical analysis

Since a shielding gas with low active and reducing shielding gas components was used and no brushing between the individual layers took place, the chemical composition of welds was determined. **Table 7** shows the values of the additive welded wall as a function of the different shielding gases in comparison with the element contents of wire batch.

An influence of shielding gas or component geometry and heat input on the chemical compositions cannot be proven. If deviations occur, they are more likely to be due to measurement inaccuracies resulting from calibration tolerances. Thus, the weld metals also show the same tendency with respect to the Nb/C ratio.

The O- and N-contents of part geometries of both batches welded with ArHeHC show a slight increase compared with the wire batches (**Figure 13**). A similar behavior is shown for the blocks produced with the different shielding gases (**Figure 14**).

However, the weld metal of the standard batch dissolves slightly more oxygen and nitrogen compared with the AM batch. In addition, the reducing effect is observed for the shielding gas with the highest H content (Ar with 2% H<sub>2</sub>). The low O<sub>2</sub> and CO<sub>2</sub> contents do not cause oxygen pickup by the weld metal.

Element	C	Si	S	Cr	Mo	Fe	Nb	Al	Ti	Cu	Co	Ni	Nb/C
standard	0.04	0.06	0.001	19.1	2.6	17.9	5.67	0.53	1.12	0.05	0.07	52.6	149
ArHeHC	0.04	0.06	0.001	19.0	2.6	17.5	5.65	0.56	1.14	0.06	0.06	53.2	145
ArHeH	0.04	0.07	0.001	18.9	2.5	17.7	5.65	0.56	1.14	0.06	0.06	53.2	149
ArH	0.04	0.07	0.001	18.9	2.5	17.7	5.63	0.56	1.14	0.06	0.07	53.2	148
ArHeO	0.04	0.07	0.001	18.9	2.5	17.7	5.60	0.55	1.14	0.06	0.07	53.4	147
AM	0.07	0.04	0.001	18.0	2.7	20.2	5.99	0.52	1.16	<0,01	<0,001	51.2	89
ArHeHC	0.07	0.03	0.001	17.8	2.9	20.2	5.80	0.54	1.08	<0.01	<0.001	51.5	85
ArHeH	0.07	0.03	0.001	17.9	2.9	20.2	5.86	0.53	1.08	<0.01	<0.001	51.3	83
ArH	0.07	0.03	0.001	18.0	2.9	20.2	5.80	0.53	1.08	<0.01	<0.001	51.2	83
ArHeO	0.07	0.03	0.001	18.0	2.9	20.2	5.83	0.53	1.08	<0.01	<0.001	51.3	84

**Table 7.**  
 Chemical composition of wire batches of S Ni 7718 blocks depending on shielding gas (wt%).

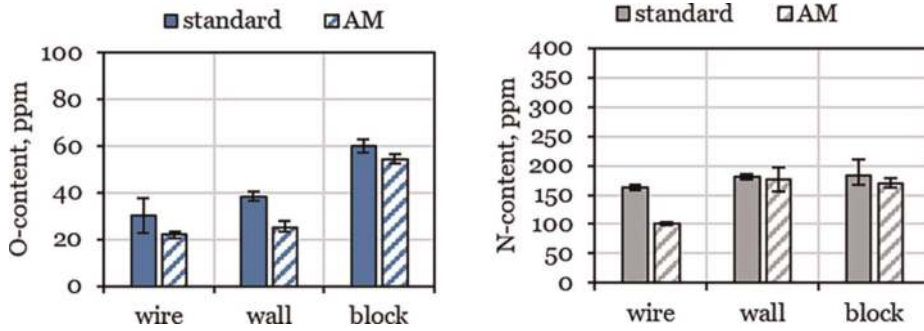


**Figure 13.** ON-contents of S Ni 7718 walls and blocks depending on wire batch (shielding gas: ArHeHC).

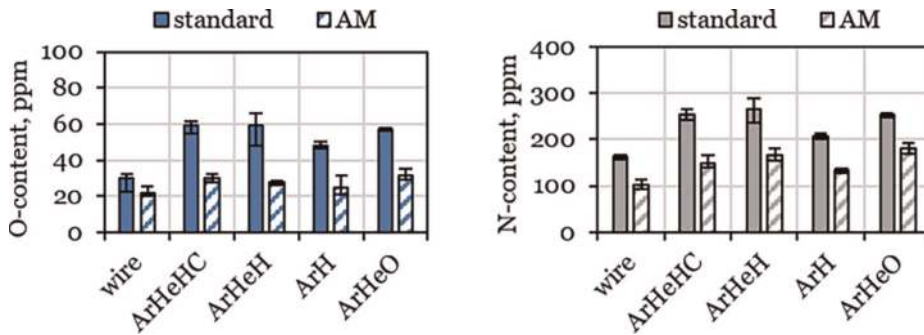


**Figure 14.** ON contents of S Ni 7718 blocks depending on shielding gas.

## 5.6 Macrostructure and defects

**Figure 15** shows the macro cross sections (Y-Z plane) of the walls of different wire batches. At constant wall height, the weld width increases with rising deposition rate and the number of layers reduces. As a result of the lower deposition rate when welding with the AM batch, more plies had to be welded to achieve equal weld heights. In addition, comparatively large thickness reductions are recorded in the lower wall structure area when welding with 6.0 m/min wire feed and 1.0 m/min travel speed. To avoid this effect, it would be necessary to adjust the wire feed speed or, if necessary, to preheat the substrate sheet, but this was not the focus of these investigations. In order to obtain an evaluation of the lateral surface waviness, the end contour proximity (ECP) was determined according to Eq. 3.

$$ECP = \frac{W_{\text{inside}}}{W_{\text{outside}}} \cdot 100 [\%] \quad (3)$$

Since the sections have been split, the lower value of the nominal wall width and the higher value of the actual wall width are relevant. During the evaluation, the upper rounded and the lower, partially constricted areas of the samples were not considered. All wall structures except one wall achieved an ECP of  $\geq 75\%$ , which is according to [31] a good value. Since the image quality indicator of the X-ray inspection is not sufficient to detect micro hot cracks, the cross sections of the walls and blocks were inspected for internal seam defect. With one exception, there were no hot cracks in the walls. Only in one cross section of the AM batch of S Ni 7718 hot cracks were separated and visible in the second and third layers (**Figure 16**).

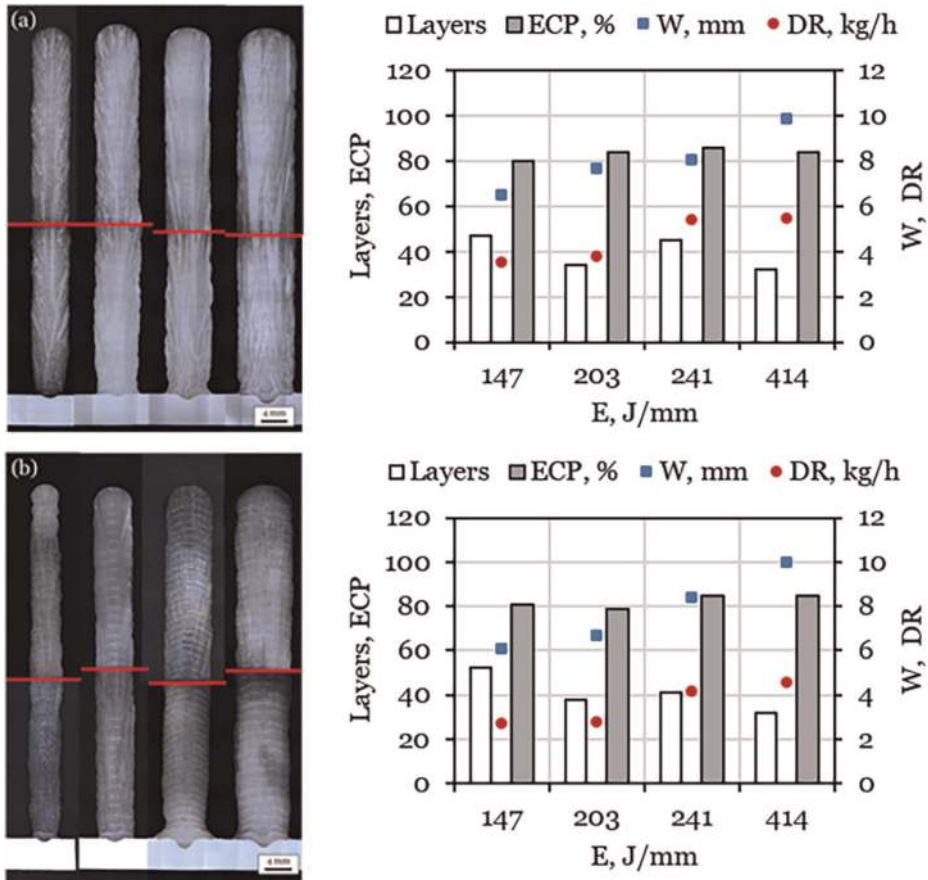


**Figure 15.** Cross sections (Y-Z plane) of S Ni 7718 walls: (a) standard (b) AM welded with ArHeNC.

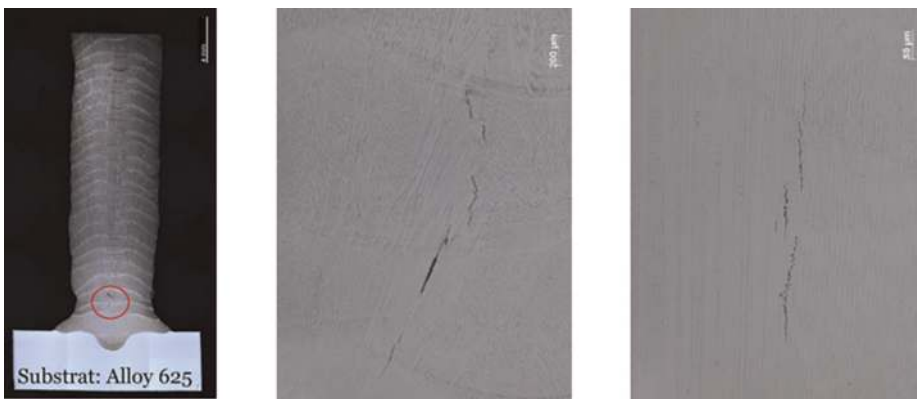
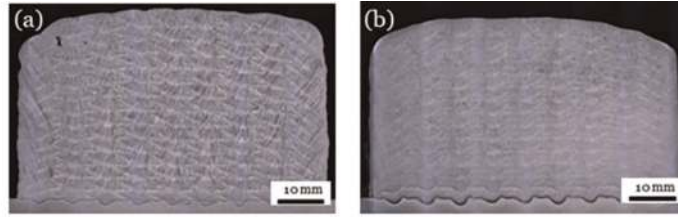


**Figure 16.** Hot cracks in the lower layers of S Ni 7718 AM wall (WFS:9.0 m/min, TS: 1.0 m/min, ArHeHC).

For the blocks, the higher welding feed speed in a wider block with the same number of layers and beads (**Figure 17**) can also be seen. The machining allowances are comparable to those of the walls. However, the ECP is very high due to the large width of the block. When the blocks are welded, lateral tracking of the beads can be observed on each side in each position. Due to this, the process is more unstable and a lot of weld spatter occurs. In principle, the wire feed speed would have to be adjusted for these weld beads, but this has not been done.



		Standard batch	AM batch
Layers / beads	[-]	9 / 126	9 / 126
H <sub>block</sub>	[mm]	42.0	39.0
W <sub>block</sub>	[mm]	57.5	60.9
ECP	[%]	97	98

**Figure 17.** Cross sections (Y-Z plane) of S Ni 7718 blocks: (a) standard, (b) AM welded with ArHeHC.

Defect	Hot crack		Lack of fusion
	Number	CL, $\mu\text{m}/\text{mm}^2$	Number
Standard	17	2.3	2
AM	83	33.3	1

**Table 8.** Defects in S Ni 7718 blocks, welded with ArHeHC.

Due to the significantly larger number of weld beads in large blocks, the thermal-mechanical reactions were higher than for the walls, so that hot cracks occurred in both blocks despite faster cooling. In addition to the hot cracks, also few lacks of fusion were also found. A quantitative evaluation of the number of cracks and the weld metal area-related crack length (Eq. 4) shows a significantly higher hot crack sensitivity of the AM batch of S Ni 7718 (**Table 8**). This confirms the investigation results of [27, 28] that a higher Nb/C ratio results in greater susceptibility to hot cracking.

$$CL = \frac{\text{Total length of cracks}}{\text{weld metal area}} \quad [\mu\text{m}/\text{mm}^2] \quad (4)$$

**Figure 18** shows the blocks produced with different shielding gases. Eq. 1 and Eq. 2 (**Figure 3**) were used here to determine the center distance  $d$  between the beads. At the side block edges, there is always a lateral flow of the melt, which leads to an uneven deposit. While the calculated center distance was set for the blocks of the AM batch, a fixed spacing of 5.5 mm was set for welding with the standard batch. This, together with the higher wire feed speed of 9.5 m/min, resulted in wider blocks with lower heights for the same number of beads per layer in the AM batch.

The evaluation of the macro sections showed for the blocks from the AM batch not only many hot cracks but also a large number of lacks of fusion (**Figure 19, Table 9**). But these defects also occurred in the blocks of the standard batch. No internal defects were visible on the walls of S Ni 7718.

## 5.7 Mechanical properties at room temperature and hardness

**Tables 10** and **11** show the mechanical properties at room temperature of S Ni 7718 walls and blocks welded with ArHeHC.

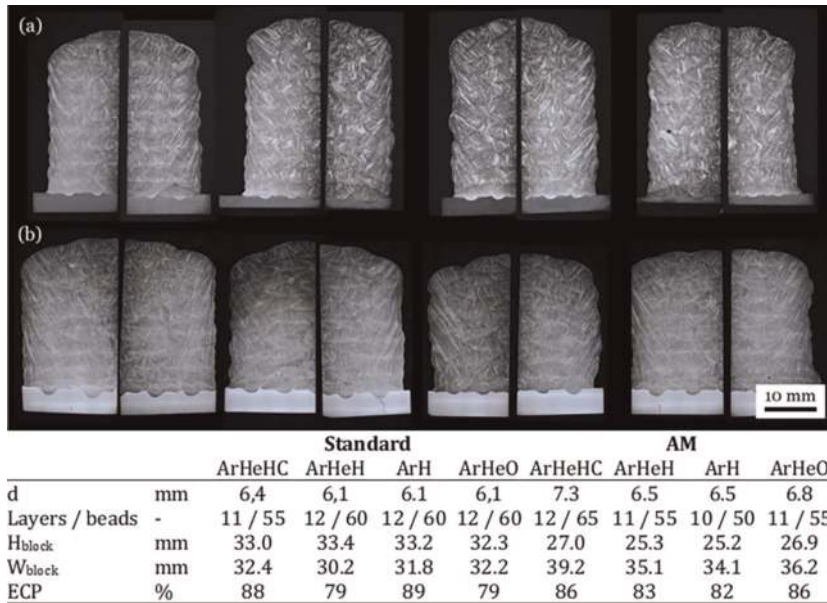


**Figure 18.**  
 Cross sections (Y-Z plane) of the block structures of S Ni 7718 batches: (a) standard (b) AM.

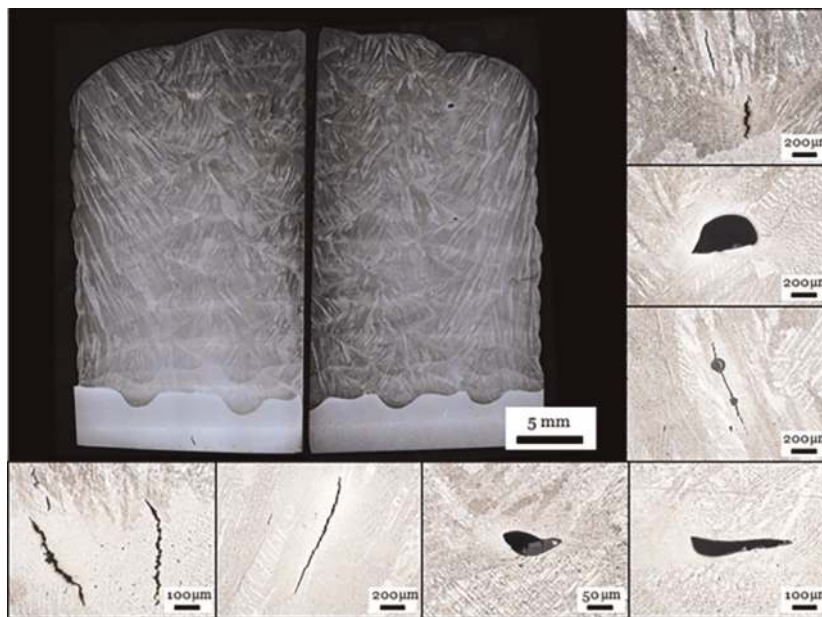


**Figure 19.**  
 Example of unacceptable defects in S Ni 7718 blocks of AM batch, welded with ArHeHC.

	Standard				AM			
	ArHeHC	AeHeH	ArH	ArHeO	ArHeHC	ArHeH	ArH	ArHeO
No. hot crack	6	5	5	6	20	11	7	13
CL, $\mu\text{m}/\text{mm}^2$	2,5	1,4	1,6	3,0	5,8	3,8	2,3	5,1
No. lack of fusion	0	0	1	3	15	13	12	8

**Table 9.**  
 Defects in S Ni 7718 blocks, welded with different shielding gases.

	Standard						AM					
E	[J/mm]	147 ± 9.1	203 ± 5.7	414 ± 9.4	241 ± 11.1	115 ± 6.1	192 ± 13.7	200 ± 6.0	388 ± 8.9			
UTS	[MPa]	767 ± 10	765 ± 10	762 ± 6	754 ± 1	759 ± 11	775 ± 8	771 ± 4	785 ± 1			
YS <sub>0.2</sub>	[MPa]	470 ± 10	488 ± 10	454 ± 4	464 ± 9	409 ± 16	499 ± 13	440 ± 15	439 ± 10			
A	[%]	42,0 ± 1.9	39,7 ± 6.0	38,9 ± 1.8	42,1 ± 5.7	39,7 ± 0.3	40,1 ± 0.7	35,5 ± 4.6	34,3 ± 0.2			
HV10	[-]	237 ± 24	244 ± 17	245 ± 22	237 ± 21	242 ± 24	249 ± 17	247 ± 16	242 ± 19			

**Table 10.** Summary of tensile properties and hardness measurements of S Ni 7718 walls (shielding gas: ArHeHC).

	UTS [MPa]	YS <sub>0.2</sub> [MPa]	A [%]	HV10	KV, 20°C [J]	KV, -196°C [J]
Standard	792 ± 2	487 ± 7	36.1 ± 3.9	271 ± 19	88.5 ± 3.5	77.5 ± 2.5
AM	792 ± 33	528 ± 14	23.6 ± 3.9	275 ± 34	65.0 ± 5.0	49.0 ± 1.5

**Table 11.**  
 Results of tensile and charpy tests as well as hardness measurements of S Ni 7718 blocks (shielding gas: ArHeHC).

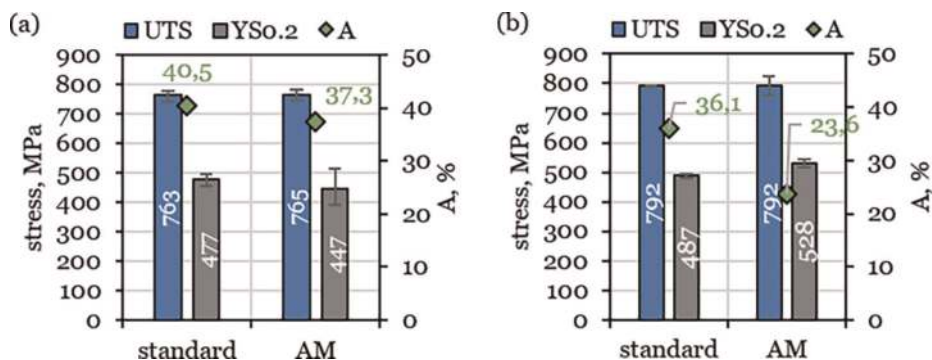


**Figure 20.**  
 Mean values of tensile properties of S Ni 7718 walls (a) and blocks (b), welded with ArHeHC.

If the influence of wire batch is considered independently of the geometry, the AM batch leads to a lower elongation at rupture (A) compared with the standard batch (**Figure 20**). The values for the 0.2% yield strength, on the other hand, behave divergently, while no significant difference occurs for the tensile strength. Considering the influence of the geometry, the blocks show a slightly higher tensile strength, 0.2% yield strength and hardness, while the elongation at rupture is significantly lower. The reasons for the higher strengths of the blocks compared with the walls are probably due to the faster cooling.

An influence of the shielding gases on the strength is not detectable (**Table 12**). The impact energy values determined scatter slightly, but a correlation with the shielding gases cannot be demonstrated (**Table 13**).

For the identification of an aging effect on the deposit hardness, local hardness maps (HV0.2) were performed over 2–3 layers in the center of the walls and blocks welded with the highest heat input (**Figure 21**). The results of the walls show no significant changes in hardness, indicating an age hardening effect.

## 5.8 Microstructure of deposit weld metals

Already on the polished cross sections of walls and blocks, a large number of irregularly distributed cubic particles are visible, which are either TiN or NbC (**Figure 22**). The nitrides containing a certain amount of Ti are already formed in the melt at a later stage of solidification [24].

The Laves phase is already clearly visible in the etched sections at the light microscope at sufficiently high magnification (**Figure 23**).

The scanning electron microscope (SEM) images demonstrate the precipitated phases in the microstructure of samples, such as Laves Phase and complex NbC, Ti N-particles (**Figure 24**).

The precipitation of these phases appeared for all walls and blocks. The brittle Laves phase is generally considered to be the major microstructural segregation

	Standard						AM					
	ArHeHC	ArHeH	ArH	ArHeO	ArHeHC	ArHeH	ArH	ArHeO	ArHeHC	ArHeH	ArH	ArHeO
UTS	[MPa]	729 ± 5	731 ± 5	738 ± 4	729 ± 4	765 ± 6	753 ± 7	756 ± 5	753 ± 7	756 ± 5	758 ± 16	
0.2 YS	[MPa]	440 ± 2	434 ± 14	438 ± 9	410 ± 22	452 ± 20	453 ± 3	452 ± 20	452 ± 20	452 ± 20	445 ± 17	
A	[%]	39.9 ± 2.7	39.2 ± 2.3	38.2 ± 1.6	41.0 ± 1.4	39.3 ± 0.9	36.2 ± 1.6	39.4 ± 2.3	36.2 ± 1.6	39.4 ± 2.3	39.3 ± 2.3	
HV10	[-]	245 ± 23	243 ± 17	248 ± 25	258 ± 14	244 ± 22	242 ± 17	247 ± 16	244 ± 22	247 ± 16	247 ± 16	

**Table 12.** Summary of tensile properties and hardness measurements of S Ni 7718 walls depending on shielding gas.

	Standard					AM					
	ArHeHC	ArHeH	ArH	ArHeO	ArHeHC	ArHeH	ArH	ArHeO	ArHeHC	ArHeH	ArH
HV10	[–]	275 ± 24	278 ± 25	282 ± 13	279 ± 15	264 ± 22	263 ± 26	266 ± 26	263 ± 26	266 ± 26	274 ± 36
KV, 20°C	[J]	77.5 ± 0.5	80.0 ± 2.0	84.0 ± 0	81.0 ± 1.0	75.0 ± 0	68.5 ± 1.5	80.0 ± 2.0	68.5 ± 1.5	80.0 ± 2.0	77.0 ± 1.0
KV, –196°C	[J]	63.5 ± 1.5	67.5 ± 1.0	66.0 ± 1.5	61.0 ± 1.0	62.0 ± 2.0	63.5 ± 0.5	61.5 ± 1.5	63.5 ± 0.5	61.5 ± 1.5	65.5 ± 2.5

**Table 13.**  
 Results of Charpy V tests and hardness measurements of S Ni 7718 blocks dependent on shielding gas.

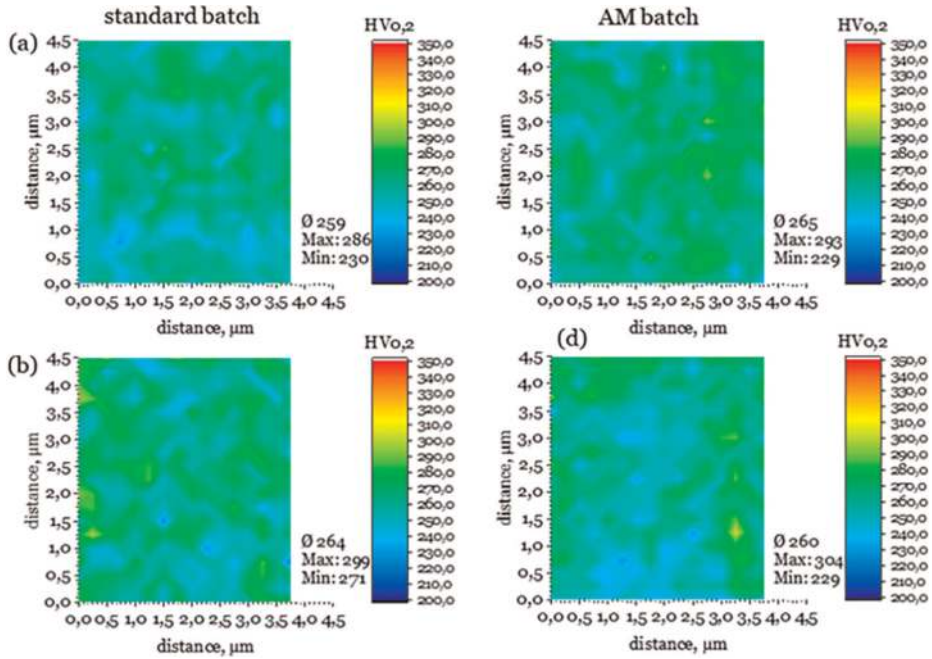


Figure 21. Hardness maps an (a) walls and (b) blocks of different wire batches of S Ni 7718.

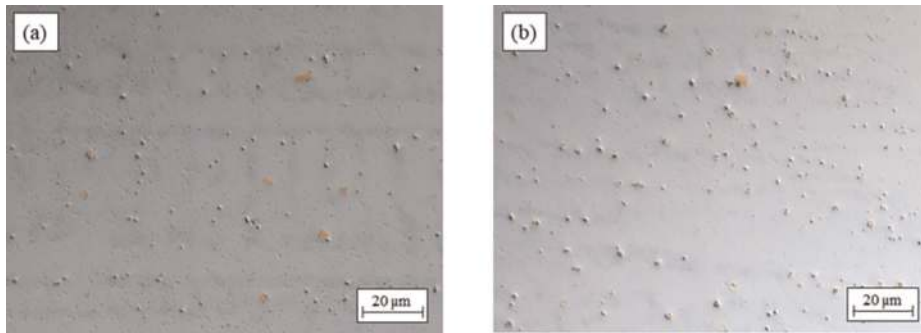


Figure 22. Light microscopic images of polished walls of S Ni 7718: (a) standard (b) AM.

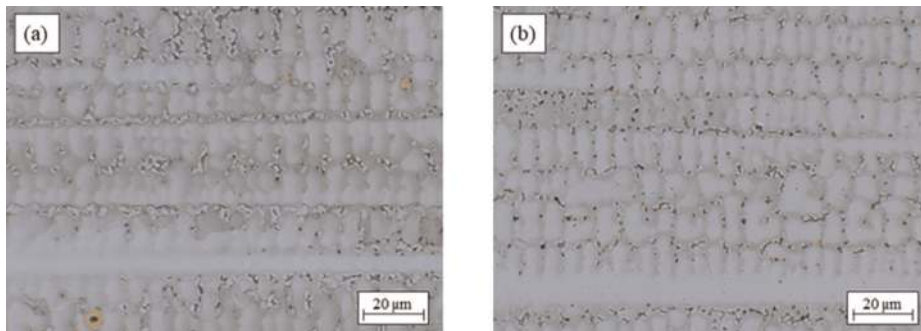
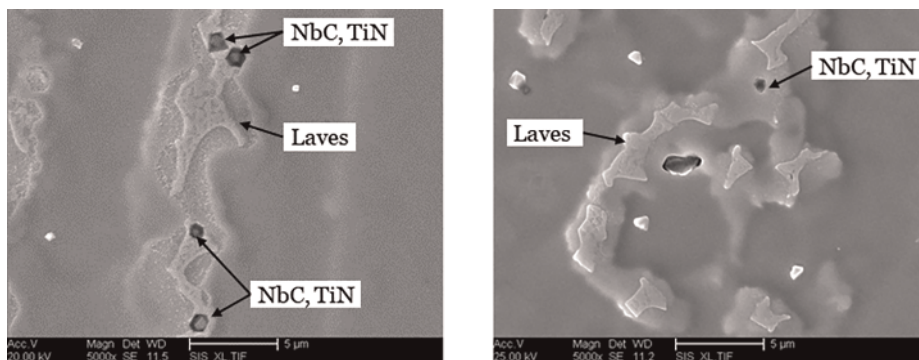


Figure 23. Light microscopic images of etched walls of S Ni 7718: (a) standard (b) AM (etchant: NaOH).



**Figure 24.**  
 SEM of etched walls of S Ni 7718: (a) standard (b) AM batch.

Elements	Nb	Mo	Ti	Cr	Fe	Ni	Phase
Standard	21.84 ± 1.01	5.23 ± 0.42	1.63 ± 0.09	13.06 ± 0.42	12.10 ± 0.28	43.14 ± 1.38	Laves
	4.42 ± 0.98	3.42 ± 0.34	1.04 ± 0.17	18.32 ± 0.36	18,0.4 ± 0.62	53,97 ± 0.50	Matrix
AM	22,27 ± 1.79	5.63 ± 0.34	1.62 ± 0.15	12.64 ± 0.17	13.29 ± 0.29	44.55 ± 0.82	Laves
	3.93 ± 0.84	3.40 ± 0.24	0.97 ± 0.14	17.75 ± 0.21	20.60 ± 0.53	52.57 ± 0.66	Matrix

**Table 14.**  
 SEM with secondary electron detector on walls of S Ni 7718: (a) standard (b) AM (wt%).

constituent of welded alloy 718. Nb and Mo are enriched in the Laves phase, whereas Al, Fe, Cr, and Ni are depleted (**Table 14**).

## 6. Conclusions

1. The chapter shows that the part geometry and the wire composition of Alloy 718 significantly affect the hot cracking tendency in CMT-WAAM weld metal. The influence of geometry is greater in this case.
2. In multilayer WAAM welds using the energy-reduced CMT process, the risk of occurrence of unacceptable lack of fusion is very high despite useful calculation tools due to the narrow beads, large wetting angles, and uneven deposition in the edge areas of components.
3. Mechanical properties of the WAAM weld metal of both batches differ only slightly. The AM batch generates slightly higher tensile strength and yield strength, but lower elongation at rupture and notched bar impact work.
4. The composition of the shielding gas mixture in CMT-WAAM welding is rather redundant in terms of improved wetting behavior of molten metal. An influence on the mechanical properties is not visible.
5. The hardness of blocks is about 30 HV 10 higher than that of walls, probably caused by increased precipitation of the brittle and hard phases (Laves, NbC, TiN). In the solution-annealed condition, the hardness is only 200 HV10.

6. The precipitation of the  $\gamma''$  and  $\gamma'$  strengthening phases in as-welded condition was not observed. But precipitates, such as Laves, NbC, TiN, which are often described in the literature, appear in the weld metal.

## **Acknowledgements**

The present contribution is a part of the AiF project IGF-No. 20.616 B/DVS-No. 01.3145 of the German Research Association on Welding and Allied Processes (DVS). It was kindly supported by the AiF (German Federation of Industrial Research Associations) within the program for promoting the Industrial Collective Research (IGF) of the Federal Ministry for Economic Affairs and Energy (BMW), based on a decision by the German Bundestag.

## **Conflict of interest**

Manuela Zinke, Stefan Burger, and Sven Juettner declare that they have no conflict of interest.

## **Author details**

Manuela Zinke\*, Stefan Burger and Sven Juettner  
Institute of Materials and Joining Technology, Otto von Guericke University,  
Magdeburg, Germany

\*Address all correspondence to: manuela.zinke@ovgu.de

## **IntechOpen**

---

© 2022 The Author(s). Licensee IntechOpen. This chapter is distributed under the terms of the Creative Commons Attribution License (<http://creativecommons.org/licenses/by/3.0>), which permits unrestricted use, distribution, and reproduction in any medium, provided the original work is properly cited. 

## References

- [1] Debarbadillo JJ, Mannan SK. Alloy 718 for oilfield applications. *JOM*. 2012;**64**: 265-270. DOI: 10.1007/s11837-012-0238-z
- [2] Paulonis DF, Schirra JJ. Alloy 718 at Pratt & Whitney—Historical perspective and future challenges. *Superalloys 718, 625, 706 and various derivatives*. 2001: 13-23. DOI: 10.7449/2001/Superalloys\_2001\_13\_23
- [3] Ezugwu E, Wang Z, Machado A. Themachinability of nickel-based alloys: A review. *Journal of Materials Processing Technology*. 1999;**86**:1-16. DOI: 10.1016/S0924-0136(98)00314-8
- [4] Kindermann RM, Roy MJ, Morana R, Prangnell PB. Process response of Inconel 718 to wire + arc additive manufacturing with cold metal transfer. *Materials & Design*. 2020;**195**:109031. DOI: 10.1016/j.matdes.2020.109031
- [5] Yilmaz O, Uгла AA. Shaped metal deposition technique in additive manufacturing: A review. *Journal of Engineering Manufacture*. 2016;**230**(10): 1781-1798. DOI: 10.1177/0954405416640181
- [6] Rodrigues TA, Duarte V, Miranda RM, Santos TG, Oliveira JP. Current Status and Perspectives on Wire and Arc Additive Manufacturing (WAAM). *Materials*. 2019;**12**:1121. DOI: 10.3390/ma1207112
- [7] Ding D, Pan Z, Cuiuri D, Li H. Wire-feed additive manufacturing of metal components: Technologies, developments and future interests. *International Journal of Advanced Manufacturing Technology*. 2015;**81**:465-481. DOI: 10.1007/s00170-015-7077-3
- [8] Näkki J. Properties of alloy 625 claddings made with laser and CMT methods. (Tampere University of Technology. Publication; Vol. 1593). Tampere, Finland: Tampere University of Technology; 2018
- [9] Solecka M, Kopia A, Radziszewska A, Rutkowski B. Microstructure, microsegregation and nanohardness of CMT clad layers of Ni-base alloy on 16Mo3 steel. *Journal of Alloys and Compounds*. 2018;**751**:86-95. DOI: 10.1016/j.jallcom.2018.04.102
- [10] Ola T, Doern FE. A study of cold metal transfer clads in nickel-base INCONEL 718 superalloy. *Materials & Design*. 2014;**57**:51-59. DOI: 10.1016/j.matdes.2013.12.060
- [11] Benoit A, Jobez S, Paillard P, Klošek V, Baudin T. Study of Inconel 718 weldability using MIG CMT process. *Sci Technol Weld Joi*. 2011; **16**(6):477-482. DOI: 10.1179/1362171811Y.0000000031
- [12] Selvi S, Vishvakshenan A, Rajasekar E. Cold metal transfer (CMT) technology - an overview. *Defence Technology*. 2018; **14**(1):28-44. DOI: 10.1016/j.dt.2017.08.002
- [13] Clark D, Bache M, Whittaker M. Shaped metal deposition of a nickel alloy for aeroengine applications. *Journal of Materials Processing Technology*. 2008; **203**:439-448. DOI: 10.1016/J.JMATPROTEC.2007.10.051
- [14] Xu X, Ding J, Ganguly S, Williams S. Investigation of process factors affecting mechanical properties of INCONEL 718 superalloy in wire + arc additive manufacture process. *Journal of Materials Processing Technology*. 2019; **265**:201-209. DOI: 10.1016/J.JMATPROTEC.2018.10.023

- [15] Seow CE, Coules HE, Wu G, Khan RHU, Xu X, Williams S. Wire + Arc Additively Manufactured Inconel 718: Effect of post-deposition heat treatments on microstructure and tensile properties. *Materials & Design*. 2019;**183**:108157. DOI: 10.1016/j.matdes.2019.108157
- [16] Van D, Dinda GP, Park J, Mazumder J, Lee SH. Enhancing hardness of Inconel 718 deposits using the aging effects of coldmetal transfer-based additive manufacturing. *Materials Science and Engineering A*. 2020;**776**:139005. DOI: 10.1016/j.msea.2020.139005
- [17] Xiong J, Zhang G, Gao H und Wu L. Modeling of bead section profile and overlapping beads with experimental validation for robotic GMAW-based rapid manufacturing. *Robotics and Computer-Integrated Manufacturing* 2013;**29**(2):417–423. DOI: 10.1016/j.rcim.2012.09.011
- [18] Wittig B, Zinke M, Jüttner S, Keil D. Experimental simulation of dissimilar weld metal of high manganese steels by arc melting technique. *Weld World*. 2017;**61**:249-256. DOI: 10.1007/s40194-017-0427-z
- [19] ISO 21920-3:2021-12. Geometrical product specifications (GPS) - Surface texture: Profile - Part 3: Specification operators. Berlin: Beuth-Verlag GmbH; 2021
- [20] DIN EN ISO 17636-1:2013. Non-destructive testing of welds - Radiographic testing - Part 1: X- and gamma-ray techniques with film. Berlin: Beuth-Verlag GmbH; 2013
- [21] DIN EN ISO 6892-1:2020. Metallic materials - Tensile testing - Part 1: Method of test at room temperature. Berlin: Beuth-Verlag GmbH; 2020
- [22] DIN 50125:2016-12. Testing of metallic materials - Tensile test pieces. Berlin: Beuth-Verlag GmbH; 2012
- [23] DIN EN ISO 6507-1:2018. Metallic Materials. Vickers Hardness Test. Test Method. Berlin: Beuth-Verlag GmbH; 2018
- [24] Knorovsky GA, Cieslak MJ, Headley TJ, Romig AD, Hammett WF. INCONEL 718: a solidification diagram. *Metallurgical Transactions A*. Oct. 1989; **20**(10):2149-2158
- [25] Antonsson T, Fredriksson H. The effect of cooling rate on the solidification of INCONEL 718. *Metallurgical and Materials Transactions B: Process Metallurgy and Materials Processing Science*. Feb. 2005;**36**(1):85-96. DOI: 10.1007/s11663-005-0009-0
- [26] Radavich JF. The physical metallurgy of cast and wrought alloy 718, SuperAlloy 718s 718. *Metall Appl*. 1989: 229-240
- [27] DuPont JN, Notis MR, Marder AR, et al. Solidification of Nb-bearing superalloys: Part I Reaction sequences. *Metallurgical and Materials Transactions A: Physical Metallurgy and Materials Science*. 1998;**29**:2785-2796. DOI: 10.1007/s11661-998-0319-3
- [28] Nakao Y, Ohshig H, Koga S, Nishihara H, Sugitani J. Effect of Nb/C on the sensitivity of liquation cracking in 24Cr-24Ni-1. SNbFe-base heat resisting alloy. *Journal of the Japan Welding Society*. 1982;**51**:989-995
- [29] Hauck G. Qualitätsanforderungen an Drahtelektroden beim Schutzgasschweißen mit Robotern. *DVS Berichte*. 1989;**118**:71-76
- [30] Tammi V, Dios M. Reibkraftmessung in Schutzgas-

Schweißbrennern – die optimale  
Drahtförderung. Binzel, Gießen:  
Sonderdruck A; 1989

[31] Witzel JMF. Qualifizierung des  
Laserstrahl-Auftragschweißens zur  
generativen Fertigung von  
Luftfahrtkomponenten [Dissertation].  
Aachen, Germany: RWTH Aachen  
University; 2015. Available from: [http://  
publications.rwth-aachen.de/record/  
463044/files/463044.pdf](http://publications.rwth-aachen.de/record/463044/files/463044.pdf)